Available online at www.sciencedirect.com
SCIENCE DIRECT
Cement and Concrete Research 36 (2006) 929–942
Cement and Concrete Research

How do polypropylene fibers improve the spalling behavior of in-situ concrete?

Matthias Zeiml *, David Leithner, Roman Lackner, Herbert A. Mang

Institute for Mechanics of Materials and Structures, Vienna University of Technology, Karlsplatz 13/202, 1040 Vienna, Austria

Received 2 December 2005; accepted 16 December 2005

Abstract

The results of a recently finished research project have shown a great influence of the amount of polypropylene (PP) fibers on the spalling behavior of concrete under fire loading. Starting from the identification of the permeability as the parameter with the greatest influence on spalling, results of permeability tests on normal-strength in-situ concrete without and with PP-fibers (1.5 kg/m^3) are presented in this paper. The values for the permeability, which are obtained for concrete pre-heated to different temperature levels, are related to the pore structure, accessible by mercury-intrusion-porosimetry (MIP) tests. The considered concrete was prepared under on-site conditions, accounting for the workability and densification when casting at the construction site. In order to illustrate the effect of the permeability of concrete with and without PP-fibers on spalling, which was experienced during the aforementioned research project, a finite-element analysis, taking the coupling between heat and mass transport into account, is performed. The so-obtained results provide insight into the risk of spalling of concrete with varying amount of PP-fibers.

Keywords: Fire; Spalling; Permeability; Polypropylene fibers; Mercury porosimetry; Workability

1. Introduction

Spalling of concrete subjected to fire is related to two phenomena. On the one hand, restrained thermal dilation results in biaxial compressive stress states parallel to the heated surface, which lead to tensile stresses in the perpendicular direction [1,2]. On the other hand, the build-up of pore pressure in consequence of vaporization of physically/chemically bound water[1] [4–8] results in tensile loading of the microstructure of heated concrete. The latter is considered to have the highest influence on spalling [9].

Recent fire experiments performed within a research project sponsored by the Austrian Federal Ministry of Transportation, Innovation, and Technology (bm.vit) and the OEBB-Infrastruktur Bau AG (formerly HL-AG, Austria) revealed that the spalling depth of concrete subjected to fire decreases with increasing amount of polypropylene (PP) fibers considered in the mix design (see Fig. 1 and [10,11]). According to the open literature (see, e.g., [8,12,13]), this phenomenon can be explained by (i) the increased permeability in consequence of melting (at $T \approx 170$ °C) and, finally, vaporization (at $T \approx 340$ °C) of the PP-fibers and (ii) by the introduction of additional interfacial transition zones (ITZ) between the fibers and the cement paste. In contrast to the amount of PP-fibers, the mode of reinforcement and the type of mechanical loading, also varied within the aforementioned research project, showed marginal influence on the spalling depth.

On basis of these observations, the permeability of concrete is considered as the main parameter influencing spalling. Fig. 2 illustrates the situation in case the permeability is not sufficient to avoid spalling: water vapor, resulting from vaporization of evaporable water at temperatures above the vaporization temperature, i.e., $T > T_{Vap}$ (with $T_{Vap} \geq 100$ °C), flows towards the heated surface through the pore system of concrete

* Corresponding author. Tel.: +43 1 58801 20240; fax: +43 1 58801 20298.
E-mail address: matthias.zeiml@tuwien.ac.at (M. Zeiml).

[1] In the following, the term "evaporable water" will be used, which is related to the weight loss of concrete when dried at 105 °C [3].

0008-8846/$ - see front matter © 2005 Elsevier Ltd. All rights reserved.
doi:10.1016/j.cemconres.2005.12.018

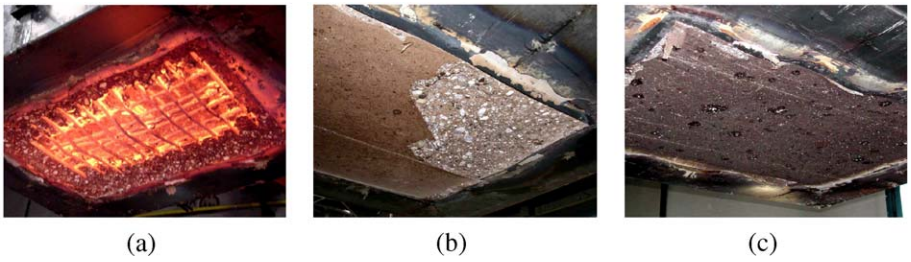

Fig. 1. Spalling depth for concrete with (a) 0, (b) 1.5, and (c) 3.0 kg/m^3 PP-fibers [10] (heated surface after 120 min of fire loading).

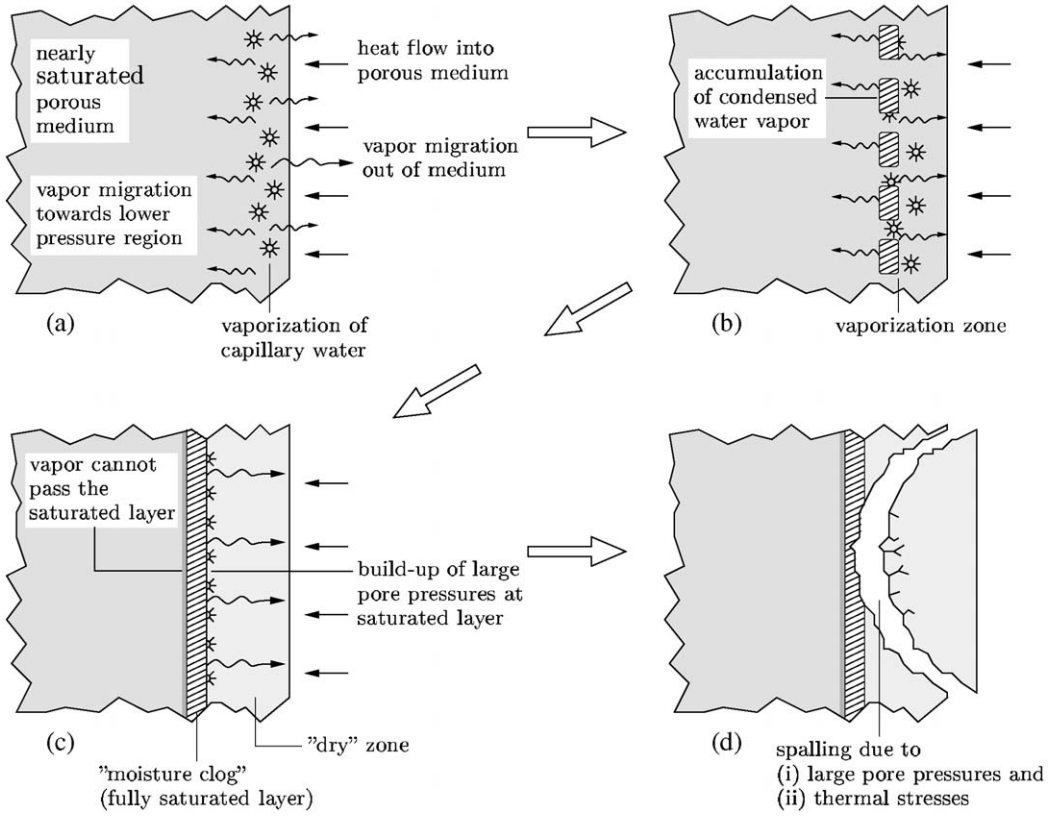

Fig. 2. Illustration of mechanism of spalling of concrete as a result of fire loading according to Refs. [6,8,14].

characterized by "dry" conditions.[2] On the other hand, water vapor flows further into the concrete structure. In regions characterized by $T \approx T_{Vap}$, the water vapor condenses again. This newly built water together with the evaporable water present in this region forms a saturated layer, acting as an impermeable wall for the gas flow ("moisture clog", see Fig. 2(c)). If the permeability of the "dry" zone of the concrete member is not sufficient to avoid a continuous pressure build-up in consequence of vaporization of evaporable water, spalling as indicated in Fig. 2(d) occurs.

So far, the determination of the permeability of concrete, changing with temperature, was restricted to laboratory-cast specimens. E.g., the influence of the amount of PP-fibers on the intrinsic permeability[3] k_{int} [m^2] for certain pre-heating temperatures was investigated in Ref. [12]. Whereas k_{int} of concrete without fibers varied two orders of magnitude (caused by dehydration of the cement paste, microcracking due to temperature-induced stresses, etc.), a variation of k_{int} by four orders of magnitude was observed for concrete with fibers within a temperature range from 80 to 400 °C. The more pronounced increase of the intrinsic permeability for concrete with PP-fibers was explained by melting of the fibers.

Accounting for the influence of on-site conditions, such as the workability of the concrete mix and densification (which are

[2] Liquid water, which would reduce the permeability of concrete, is not present in this region.

[3] k_{int} is an intrinsic parameter describing the pore space of a material, which is independent of the medium flowing through the porous material. For compressible media (e.g., air or water vapor), the intrinsic permeability is defined as the permeability at infinite pressure, with $1/p=0$.

apparently influenced by the allowance of PP-fibers), the permeability of core samples taken from large-scale specimens, cast under in-situ conditions, is investigated in this paper. Accordingly, the obtained results (presented in Section 2) can be considered as representative for concrete installed at the construction site, e.g., as tunnel lining. In order to account for the wide range of permeabilities observed during testing of pre-heated concrete, a new experimental setup was employed. In Section 3, the determined values for the permeability serve as input for the re-analysis of the experimental results obtained within the mentioned research project. For this purpose, coupled thermo-hydro-chemical finite-element simulations are performed. In Section 4, a simple scheme for estimating the water vapor production, on the one hand, and the possible advection of water vapor towards the heated surface, on the other hand, is presented. Finally, the imbalance between the production and advection of water vapor is used to assess the risk of spalling of concrete subjected to fire loading.

2. Permeability testing of pre-heated concrete

The specimens considered for permeability testing were obtained from concrete blocks (1.80 × 1.40 × 0.50 m, cast under on-site conditions with concrete used for water-proof tunnel linings, see Fig. 3), which were subjected to fire experiments as reported in Refs. [10,11]. Hereby, concrete without and with 1.5 (kg PP-fibers)/(m^3 concrete) was considered (see Table 1 for the mix design). The PP-fibers had a diameter of approximately 18 μm and a length of 6 mm (see Fig. 4).

The specimens with a height of 50 mm were obtained by cutting cores with a diameter of 143 mm, which were taken from parts of the concrete blocks not affected by the fire load (see Fig. 5(a)).

Table 1
Mix design of concrete B30/300(56)/SA/WU/LST/FB/PB/WDI [equal to C25/30(56)/WDI] [10]

Cement CEM I (PZ 375 HS) [kg/m^3]	260
Additive (fly ash) [kg/m^3]	60
Liquefier P1 [kg/m^3]	3.10
Superplasticizer SP [kg/m^3]	3.49
Air-entrainer Readyair [kg/m^3]	0.90
Water [kg/m^3]	157
Water/cement-ratio [–]	0.60
Water/binder-ratio [–]	0.49
Initial density [kg/m^3]	2386
28d-concrete density ρ_c [kg/m^3]	2362
Aggregates [kg/m^3]	1909
Aggregate fraction 0–4 mm [mass-%]	45
Aggregate fraction 4–16 mm [mass-%]	36
Aggregate fraction 16–32 mm [mass-%]	19
Aggregate mineralogy:	
Quartz [mass-%]	90
Feldspar [mass-%]	5
Carbonate [mass-%]	5

Definitions according to Ref. [15]:
SA … Sichtbeton, auβen [exposed concrete, exterior].
WU … wasserundurchlässig [water-proof].
LST … stark lösender Angriff [severe leaching attack].
FB … frostbeständig [frost resistant].
PB … Pumpbeton [pumpable concrete].
WDI … wasserdichte Innenschale [water-proof tunnel lining].

2.1. Test procedure

The permeability tests were performed on specimens with no heat treatment (20 °C) and after pre-heating to temperatures of 80, 105, 140, 200, 300, 400, and 600 °C. All specimens were subjected to two permeability tests. Hereby, the first test was performed either at 20 °C or after pre-heating to 80 °C, whereas the second test was performed after pre-heating to a temperature between 105 and 600 °C.

The specimens were heated with a heating rate of 1 °C/min until the specified pre-heating temperature was reached. The rather slow temperature increase was chosen to avoid large temperature gradients in the specimen and, hence, severe microcracking, which would have altered the experimental results. In order to ensure that the pre-heating temperature was reached everywhere within the specimen, the samples were

Fig. 3. Casting of large-scale specimens for fire experiments under on-site conditions [10].

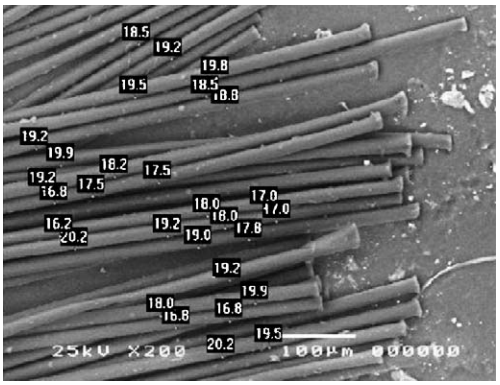

Fig. 4. Electron-microscope image showing PP-fibers considered in the mix design [10] (numbers in boxes indicate diameter [µm] of respective fibers).

stored at the respective pre-heating temperature for time spans up to 90 h. Thereafter, the temperature was reduced with a cooling rate of 1 °C/min.

After pre-heating, the specimen was prepared for permeability testing at room temperature. The lateral surface of the cylindrical specimen was sealed with wax in order to assure a one-dimensional air flow from the top to the bottom of the specimen. Then, the specimen was placed in a steel ring and both wax and acrylic were placed at the part of the specimen connected to the supporting steel ring (see Fig. 5(b)). The concrete specimen together with the steel ring was placed in the pressure chamber (see Fig. 5(c)). After fixation of the steel ring, the pressure chamber was closed at the top and the experiment was conducted at room temperature.

At the beginning of the permeability tests, the pressure in the system (at the top of the specimen) was increased to 8 bar (=0.8 MPa) and maintained sufficiently long in order to establish a constant pressure gradient and a stationary air flow through the specimen. Thereafter, the air supply was closed and the decrease of pressure by air flow through the specimen was recorded.

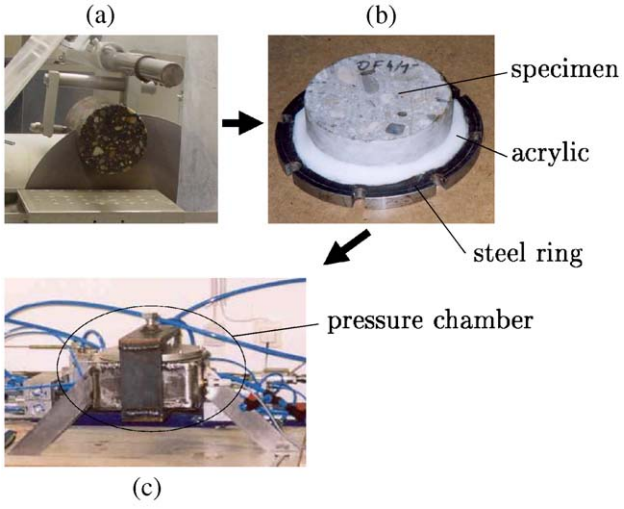

Fig. 5. Specimen preparation (a) before pre-heating and (b) before the permeability test; (c) experimental device used for permeability tests [16].

2.2. Results

Taking into account the so-called slip-flow effect in case of compressible flow in porous media [17], the permeability k [m^2] is given as a function of the intrinsic permeability k_{int} [m^2] and the so-called slip-flow constant b [Pa], reading

$$k = k_{\text{int}}\left(1 + \frac{b}{p}\right), \tag{1}$$

where p [Pa] is the air pressure in the concrete specimen. Both k_{int} and b were determined by solving the one-dimensional (non-linear) transport problem over the height of the specimen, starting from Darcy's law multiplied by $p(x)$, reading

$$p(x)Q(x) = \frac{k_{\text{int}}A}{\eta}\frac{\mathrm{d}p}{\mathrm{d}x}[p(x) + b], \tag{2}$$

and considering the pressure history at the top and bottom surface of the specimen [16]. In Eq. (2), $p(x)$ [Pa] and $Q(x)$ [m^3/s] are air pressure and air flux, respectively, at depth x [m] of the specimen, A [m^2] is the specimen surface area, and η [Pa s] is the dynamic viscosity of air. For the solution of the transport problem (2), an iterative numerical scheme is employed [16].

The so-obtained intrinsic permeability k_{int} is shown in Fig. 6 for concrete specimens without PP-fibers. The large variation of the test results corresponding to pre-heating temperatures of 20 and 80 °C is explained by the evaporable water still present at these temperatures. With increasing pre-heating temperature, the evaporable water is removed and the obtained results show less scatter. As expected, an increase of the pre-heating temperature results in an increase of the intrinsic permeability.

This trend is also observed for the permeability obtained from testing of concrete with PP-fibers (see Fig. 7). Compared to the results of concrete without PP-fibers, the scatter of the obtained results at lower pre-heating temperatures is significantly smaller and the permeability values are higher (see, e.g., results for T=20 °C).

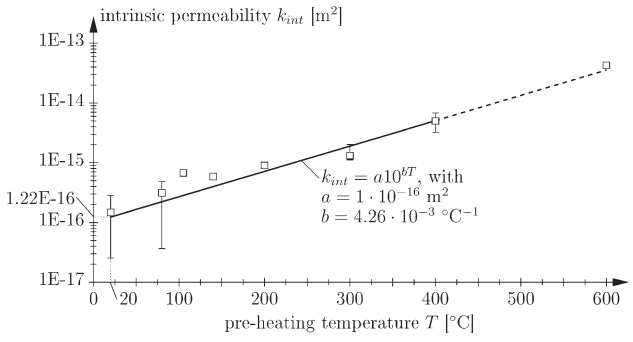

Fig. 6. Experimentally obtained intrinsic permeability for concrete specimens with 0 kg/m^3 PP-fibers (squares represent average values, lines mark minimum and maximum value).

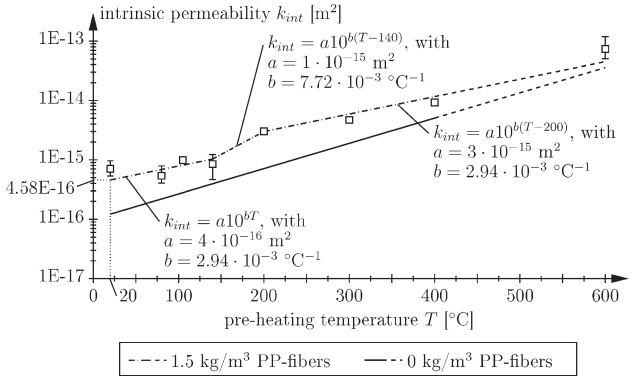

Fig. 7. Experimentally obtained intrinsic permeability for concrete specimens with 1.5 kg/m³ PP-fibers (squares represent average values, lines mark minimum and maximum value).

2.3. Discussion

In contrast to the approximation of the intrinsic permeability of concrete without PP-fibers by *one* linear function in the *T*-log (k_{int})-diagram (Fig. 6), the permeability for concrete with 1.5 kg/m³ PP-fibers is approximated by a tri-linear function (see Fig. 7). Based on these approximation functions, the following conclusions can be drawn:

(1) At temperatures lower than 140 °C, the permeability of concrete with PP-fibers is found to be three to four times larger than the permeability of concrete without fibers (see Fig. 7), with a decreasing difference for increasing pre-heating temperatures. This difference is significantly higher than in respective experimental results found for laboratory-cast specimens presented in [12]. This discrepancy between in-situ and laboratory-cast concrete can be explained by
- the introduction of additional ITZ at casting, associated with PP-fibers [8,13], which could be of higher influence in case of in-situ concrete due to various on-site conditions;
- the reduced on-site workability and the lower effect of densification [10], influencing the pore structure of the in-situ concrete and/or the characteristics of the ITZ (e.g., internal bleeding in consequence of a higher amount of liquefier influences the formation of ITZ [10]); and
- the different cracking behavior of concrete with and without PP-fibers during curing (see, e.g., [18–21]). Experiments performed on pre-heated concrete [12] revealed a much higher crack density in case of heated fiber-reinforced concrete compared to heated concrete without PP-fibers. Hereby, the cracks of the latter showed larger crack widths. The improved connectivity of the crack network in case of fiber-reinforced concrete may also contribute to the higher permeability at temperatures below 100 °C.

In summary, the higher low-temperature permeability shown in Fig. 7 explains the improved spalling behavior of concrete with PP-fibers below the melting temperature of the PP-fibers ($T \approx 170$ °C), i.e., within 100 °C $\leq T \leq$ 170 °C, when the evaporable water in the pore system is already vaporizing.

(2) For temperatures between 140 and 200 °C, the difference between the permeability of the investigated types of concrete increases (see Fig. 7), reaching again a factor of four (as observed for low-temperature results). In contrast to experimental results obtained for laboratory-cast concrete [12], showing the maximum in the difference between the permeability for concrete with and without fibers at a pre-heating temperature of 200 °C, which is close to the melting temperature (T=171 °C) of the fibers used in the respective experiments, this effect was smaller for the considered in-situ concrete. At the most, its influence was of equal importance as the aforementioned difference in the low-temperature permeability.

(3) Above 200 °C, the difference in permeabilities decreases in a similar manner as for temperatures below 140 °C, indicating that temperature-induced damage of the concrete reduces the overall effect of the PP-fibers on the permeability.

(4) For specimens pre-heated to 600 °C, severe damage of the investigated specimens was observed. Accordingly, in the pre-heating temperature range from 400 to 600 °C, the obtained results are less exact and strongly affected by cracks opening during heating/cooling, as indicated by the dashed lines in Figs. 6 and 7.

In order to explain the observed characteristics of the intrinsic permeability, which strongly depend on the actual pore structure of concrete, mercury-intrusion-porosimetry (MIP) experiments were performed on small concrete samples subjected to the same pre-heating temperatures as the permeability specimens (i.e., T=20, 80, 105, 140, 200, 300, 400, and 600 °C). Since the mercury pressure of the employed MIP device is limited, only a specific range of pore radii (1.9 nm $\leq r \leq$ 75 μm) can be detected. Moreover, because of the rather small sample size, only the presence of low-size aggregates is taken into account, disregarding the influence of the ITZ of larger-size aggregates.

Considering the total pore volume obtained from MIP testing, which shows an increasing behavior with increasing temperature (see Fig. 8), the rather small difference between

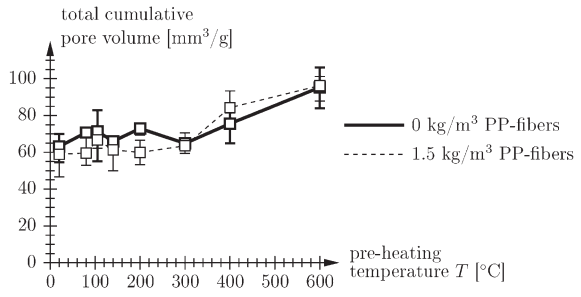

Fig. 8. MIP results: total cumulative pore volume of concrete after exposure to different temperatures [22] (squares represent average values, lines mark minimum and maximum value).

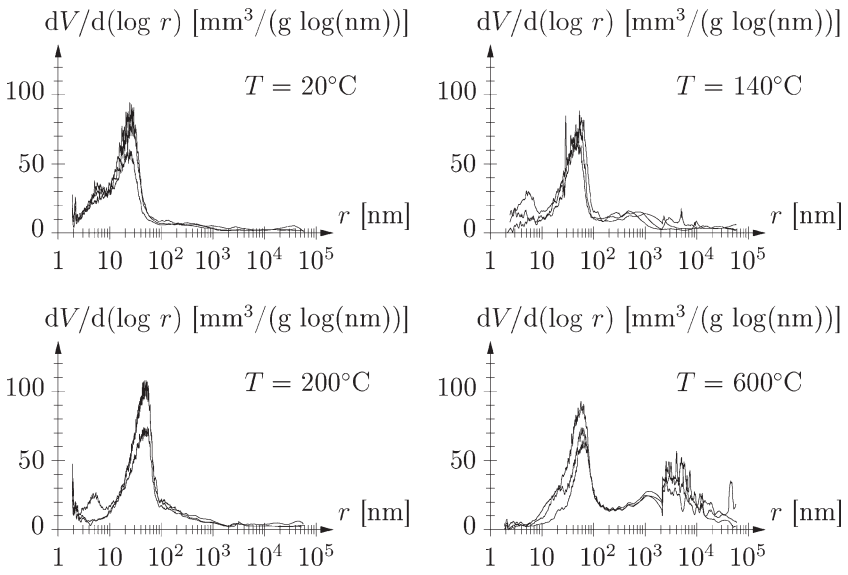

Fig. 9. MIP results: dV/d(log r) of samples of concrete with 0 kg/m^3 PP-fibers after exposure to different temperatures [22].

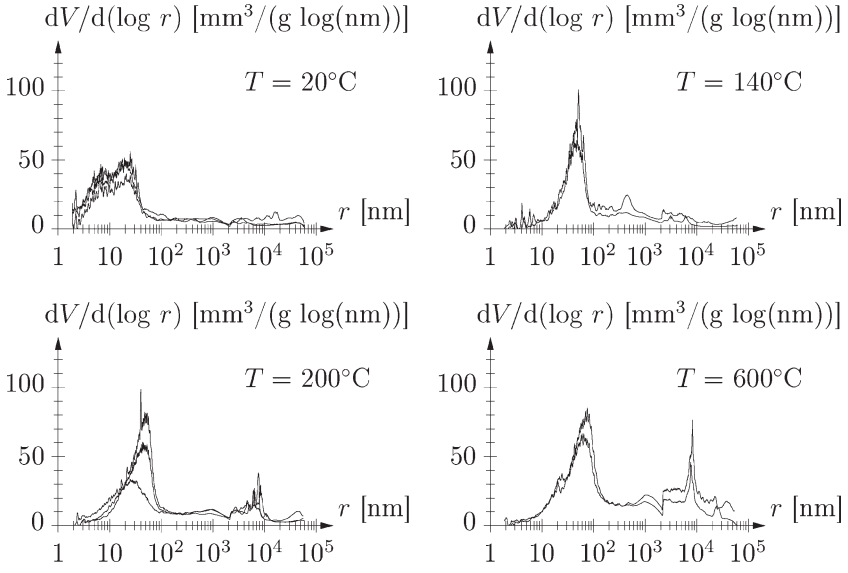

Fig. 10. MIP results: dV/d(log r) of samples of concrete with 1.5 kg/m^3 PP-fibers after exposure to different temperatures [22].

concrete with and without fibers cannot explain the higher permeability of fiber-reinforced concrete obtained from the permeability tests. As regards the obtained pore-size distributions, an almost similar development for concrete with and without PP-fibers is observed (see Figs. 9 and 10). In both cases, the peak within the pore-size range of $10 \le r \le 100$ nm is shifted towards larger radii for increasing pre-heating temperature. In case of concrete with 1.5 kg/m^3 PP-fibers, this peak is less pronounced for T=20 and 80 °C and the largest shift of this peak towards larger pore radii is observed between pre-heating temperatures of 80 and 105 °C. Within the pore-size range of $6 \le r \le 10$ μm, the pore volume of concrete with 1.5 kg/m^3 PP-fibers increases (see Fig. 10), originating from melting and, finally, evaporation of PP-fibers ($\phi \approx 18$ μm, see Figs. 4 and 11). The respective peak in the pore-size distribution starts to develop between pre-heating temperatures of T=140 and 200 °C, which corresponds to the melting temperature of the fibers at $T \approx 170$ °C [22].

The difference between concrete with and without PP-fibers at lower temperatures is highlighted by considering the change of certain pore-size ranges with temperature. As shown in Fig. 12(a) and (b), the low-temperature values of the pore volume for fiber-reinforced concrete are almost twice as large as the respective values for concrete without fibers for pore radii within[4] 10^3–10^4 and 10^4–10^5 nm (the maximum value for concrete with PP-fibers for pore radii within 10^4–10^5 nm being even three times as large as the average value for concrete without fibers). This pore-size range includes the thickness of the interfacial transition zones (ITZ) which, according to Ref. [23], is controlled by the median size of the cement grains (typically

[4] No distinct differences were observed for smaller-size pores [22].

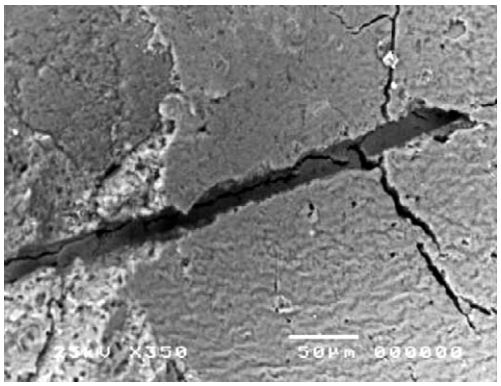

Fig. 11. Electron-microscope image of concrete pre-heated to a temperature above the vaporization temperature of polypropylene showing an empty fiber channel [10].

10–20 μm [24]). Because of the rather small sample size, only small aggregates are considered during MIP testing, disregarding the larger porosity of the ITZ of larger-size aggregates.

The effect of melting and evaporation of PP-fibers can be observed in the volume of pores with $10^3 \le r \le 10^4$ nm. Whereas the pore volume in this range remains almost constant until 200 °C for concrete without fibers, the pore volume of concrete with 1.5 kg/m^3 PP-fibers is continuously increasing (see Fig. 12(a)). For T>200 °C, both types of concrete show an increase in the pore volume of this pore-size range with increasing temperature, with no pronounced difference.

3. Re-analysis of results from large-scale fire experiments

The permeability experiments described in the previous section were performed on specimens which were obtained from the concrete blocks considered in the mentioned large-scale fire experiments (referred to as specimens VK29 to VK32 [10]). The temperature histories which were monitored in the course of these fire experiments are depicted in Figs. 13 and 14. In contrast to the specimens with PP-fibers considered in the mix design, the specimens with no PP-fibers experienced severe spalling, resulting in the destruction of temperature sensors when the spalling front reached the respective depths (indicated by a sharp increase of the respective temperature history in Fig. 13). The deviations between temperatures monitored by sensors that were placed at the same depth, but different location (see Fig. 14), are explained by local moderate spalling (up to 20 mm, see Fig. 1(b)) and the spatial variation of fire loading within the furnace.

The temperature histories from specimens VK31 and VK32 (Fig. 14) were used for re-analysis of the fire experiments employing a finite element (FE) model taking the coupled heat and mass transport in heated concrete into account (see Appendix A, Eqs. (A.1)–(A.3), and, e.g., Refs. [25–28]). Based on the geometrical properties and the loading conditions found in both large-scale fire experiments and during tunnel fires, a one-dimensional FE model was employed. For the numerical simulation, the experimental results from the respective fire experiments and from experiments reported in Refs. [29–31], which were conducted under comparable experimental conditions (fire loading, characteristics of furnace, etc.), were used to estimate the surface temperature as a function of time (see Fig. 15).

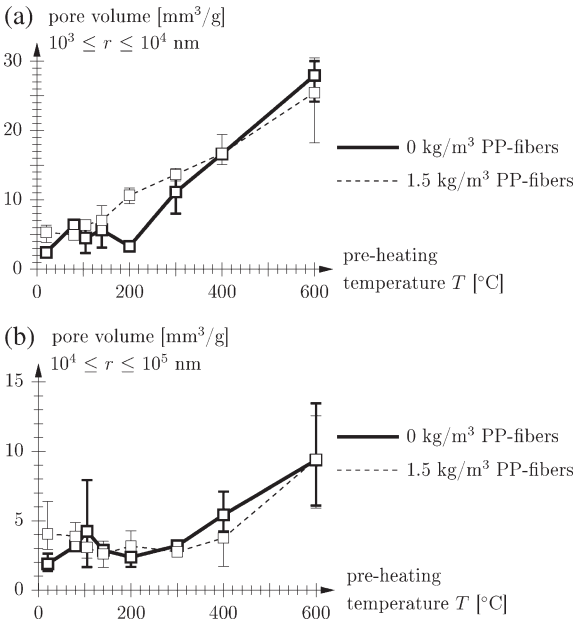

Fig. 12. MIP results: pore volume for certain ranges of pore radii after exposure to different temperatures [22] (squares represent average values, lines mark minimum and maximum value).

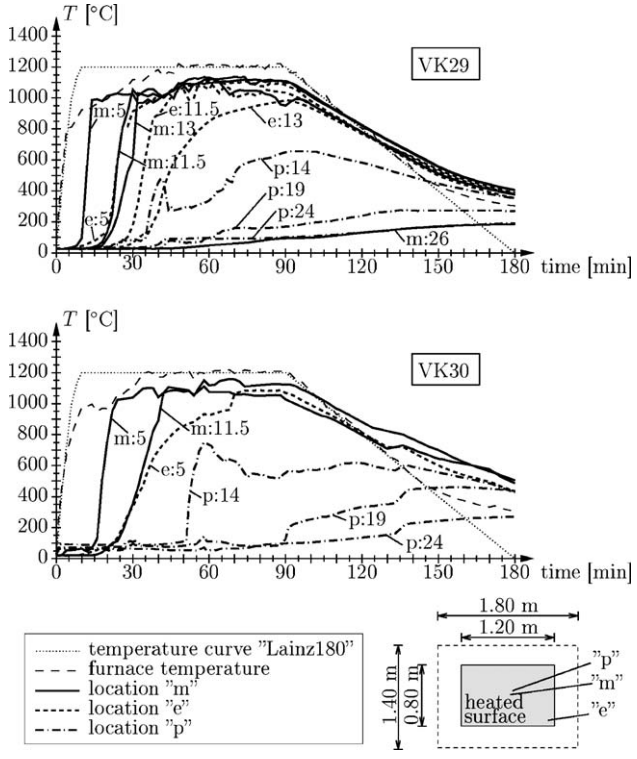

Fig. 13. Temperature histories inside the furnace and within the specimen for specimens VK29 and VK30 made of concrete with 0 kg/m^3 PP-fibers [10]; the numbers assigned to the different curves refer to the distance [cm] between the temperature sensor and the bottom surface of the concrete block.

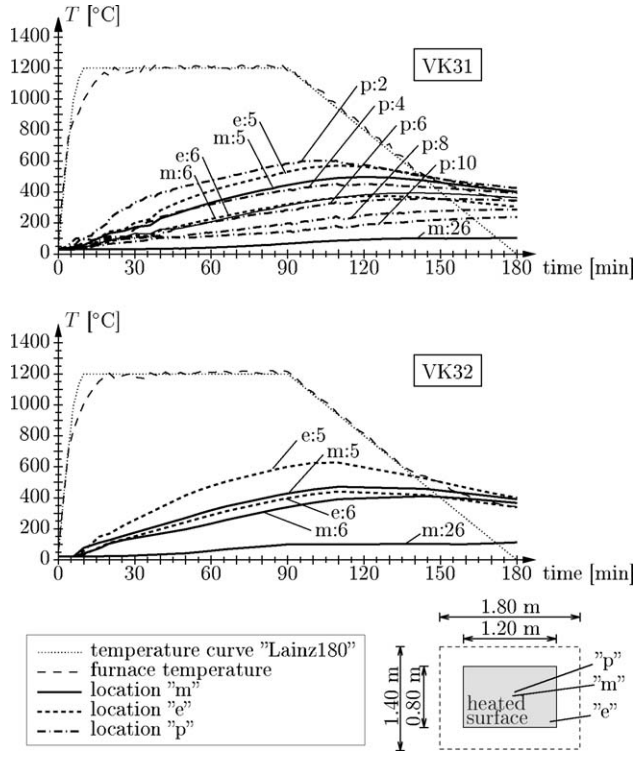

Fig. 14. Temperature histories inside the furnace and within the specimen for specimens VK31 and VK32 made of concrete with 1.5 kg/m^3 PP-fibers [10]; the numbers assigned to the different curves refer to the distance [cm] between the temperature sensor and the bottom surface of the concrete block.

In the re-analysis of the fire experiments the material parameters given in Tables 2 and 3 were used. Fig. 16 shows comparison of numerical results obtained from the analyses with experimental temperature measurements after 30 min of fire loading (only the results for the first 20 cm of the 50 cm thick specimen are shown). Whereas the results from the thermal analysis (dash-dotted line in Fig. 16, disregarding dehydration, vaporization of evaporable water, and mass transport) agree well with temperature measurements at depths of 5 and 6 cm, they overestimate the experimental results in

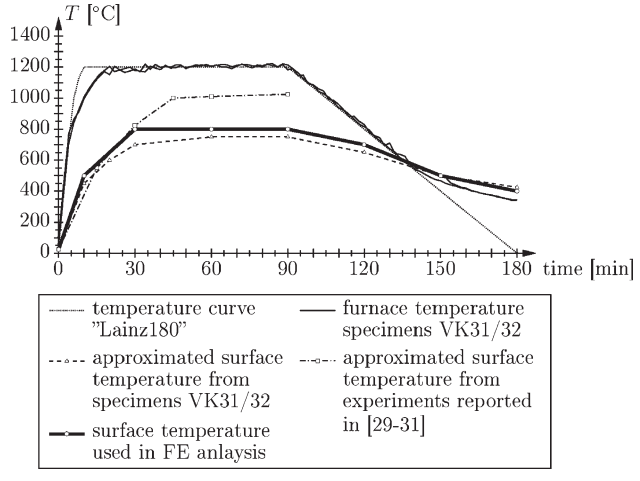

Fig. 15. Temperature loading of specimens VK31 and VK32 [10] and history of the surface temperature used in numerical analyses (thick line).

Table 2
Input parameters for the re-analysis of large-scale fire experiments [10]

Input parameter	Value	Source
Initial concrete and boundary temperature T_0 [°C]	20	–
Temperature loading	"Lainz180"	Fig. 15
Thermal conductivity λ [kJ/(h m K)]	6.48	[32]
Density ρ_c [kg/m^3]	2362	[10]
Specific heat capacity c_p [kJ/(kg K)]	1.00	[32]

2 and 4 cm depth from the heated surface. The coupled analyses, on the other hand, give the best agreement with the experimental measurements in shallow regions. Moreover, they capture the curvature of the experimentally observed temperature distributions. According to the numerical results, disregarding dehydration, vaporization of evaporable water, and mass transport results in an overestimation of the temperatures of up to 80% (see Fig. 17, the differences in temperatures are up to 156 °C). The larger impact, however, had the prescription of the surface temperature: Fig. 17 shows that prescribing the furnace temperature (referred to as "Lainz180", see Fig. 15) at the heated surface results in an overestimation of the temperatures of up to 240% (dotted line in Fig. 17, temperature differences are up to 520 °C). Comparison of the results from the coupled analyses reflects the increased mass transport in concrete with 1.5 kg/m^3 PP-fibers, resulting in increased cooling of shallow regions (with, however, rather small deviations of up to 8 °C or, equivalently, up to 5%).

In addition to temperature distributions given in Fig. 16, the coupled analyses provide also access to gas pressure and saturation distributions within the concrete block. The latter are depicted in Fig. 18 (again, only the results for the first 20 cm of the 50 cm thick specimen are shown). Whereas the saturation exceeds the initial value of 40% in case of concrete without PP-fibers, indicating the formation of a moisture clog, the permeability is sufficient to avoid this phenomenon in case of fiber-reinforced concrete. This different behavior regarding mass transport affects also the pressure distribution within the concrete block (see Fig. 19). The smaller permeability of concrete with 0 kg/m^3 PP-fibers results in a pressure rise of

Table 3
Temperature-dependent input parameters for the coupled re-analysis of large-scale fire experiments [10]

Input parameter	Initial value (at T_0=20 °C)	Temperature dependence
Thermal conductivity λ [kJ/(h m K)]	6.72	$\lambda=\lambda_0-0.006(T-T_0)$ for $T<800$ °C
Density ρ_c (ρ_s) [kg/m^3]	2362	$\rho=\rho_0+0.3(T-T_0)$
Specific heat capacity c_p [kJ/(kg K)]	0.90	$c_p=c_{p0}+0.0005$ $(T-T_0)$ for $T<T_{crit}=374$ °C
Porosity n [–]	0.142	$n=n_0+0.0001$ $(T-T_0)$
Intrinsic permeability k_{int} of concrete with 0 kg/m^3 PP-fibers [m^2]	$1.22\cdot10^{-16}$	See Fig. 6
Intrinsic permeability k_{int} of concrete with 1.5 kg/m^3 PP-fibers [m^2]	$4.58\cdot10^{-16}$	See Fig. 7
Slip-flow constant b [Pa]	$1\cdot10^5$	– (see Ref. [16] for details)

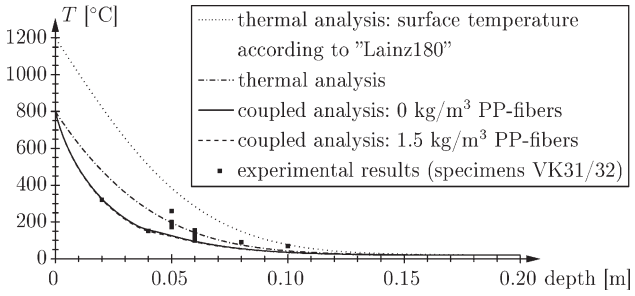

Fig. 16. Comparison of temperature distributions at $t=30$ min (PP-fibers are affecting the transport properties only. Hence, the amount of fibers has no effect on the results of the thermal analyses.).

3.3 bar above atmospheric pressure, which is almost twice as large as in case of concrete with 1.5 kg/m^3 PP-fibers, where the gas pressure exceeds the atmospheric pressure by about 1.7 bar.

4. Assessing the risk of spalling

In order to assess the influence of the permeability of concrete on the spalling behavior, an analysis tool based on the numerical results presented in the previous section is developed. As illustrated by the numerical results, the temperature prescribed at the heated surface has the largest impact on the temperature distribution. Accordingly, the surface temperature depicted in Fig. 15 (thick line) is considered in the presented analysis tool, while water and vapor transport are disregarded. Thus, the analysis tool can be divided into two parts:

(1) In the first part, the thermal problem is solved based on the analytical solution for a temperature jump from T_0 to $\bar{T}$ at $x=0$ ($x=0$ refers to the heated surface). The respective solution is given by (see, e.g., Refs. [33–35])

$$T(x,t) = T_0 + \left(\bar{T} - T_0\right) \cdot \operatorname{erfc}\left(\frac{x}{2\sqrt{at}}\right), \tag{3}$$

where erfc($\cdot$) is the Gaussian complementary error function and $a=\lambda/(\rho_c c_p)$ [m^2/s] is the thermal diffusivity.

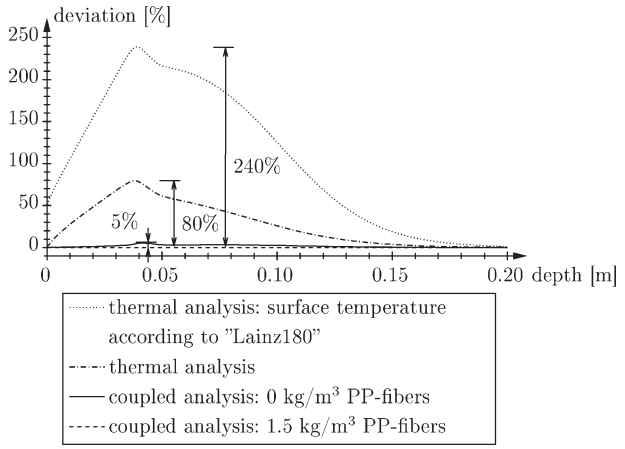

Fig. 17. Deviation between numerically obtained temperature distributions at $t=30$ min and the respective temperature distribution obtained from the coupled analysis of concrete with 1.5 kg/m^3 PP-fibers.

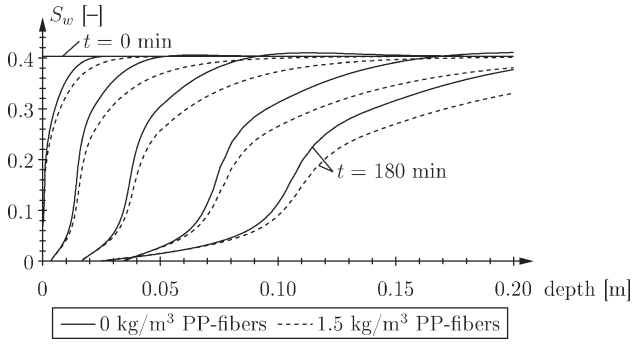

Fig. 18. Saturation distributions for concrete with 0 and 1.5 kg/m^3 PP-fibers (results for $t=0$, 2, 10, 30, 90, 180 min).

For the simulation of a tunnel fire, Solution (3) is extended to a linear temperature increase at $x=0$, reading $\bar{T}=T_0+ct$. Hereby, the surface temperature used in the previous section (thick line in Fig. 15) is considered for[5] $0\le t\le 15$ min. Based on the Duhamel's theorem (see, e.g., Ref. [34]), the infinitesimal change of the temperature field in consequence of an infinitesimal increase of the boundary temperature $\bar{T}$ can be written as

$$\mathrm{d}T(x,t) = \mathrm{d}f(\tau)\cdot F(x,t-\tau) \tag{4}$$

with

$$\mathrm{d}f(\tau) = c\cdot\mathrm{d}\tau \text{ and } F(x,t-\tau) = \operatorname{erfc}\left(\frac{x}{2\sqrt{a(t-\tau)}}\right). \tag{5}$$

Integration of Eq. (4) over time gives

$$\begin{aligned} T(x,t) &= T_0 + \int_0^t \frac{\mathrm{d}T}{\mathrm{d}\tau}\mathrm{d}\tau = T_0 + \int_0^t \frac{\mathrm{d}f(\tau)}{\mathrm{d}\tau}\cdot F(x,t-\tau)\mathrm{d}\tau \\ &= T_0 + \int_0^t c\cdot\operatorname{erfc}\left(\frac{x}{2\sqrt{a(t-\tau)}}\right)\mathrm{d}\tau. \end{aligned} \tag{6}$$

Eq. (6) allows us to trace the location of a certain T-isotherm, x_T [m] (with $T\ge 100$ °C), by solving

$$\begin{aligned} &T_0 + \int_0^t c\cdot\operatorname{erfc}\left(\frac{x_T}{2\sqrt{a(t-\tau)}}\right)\mathrm{d}\tau = T = \text{const.} \\ &\rightarrow x_T = x_T(t). \end{aligned} \tag{7}$$

Eq. (7) is solved iteratively, giving the location of the T-isotherm as a function of time and, thus, the velocity of the respective isotherm, v_T [m/s].

(2) In the second part, the water vapor distribution is determined assuming the instantaneous vaporization of

[5] Since spalling started within $3\le t\le 15$ min after the start of the fire experiments described in Ref. [10], the first 15 min of fire loading are considered appropriate for identification of the risk of spalling.

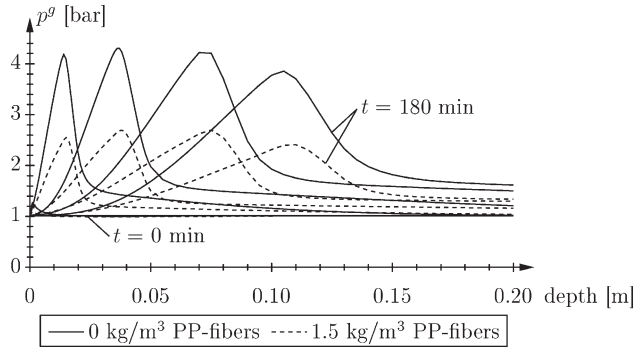

Fig. 19. Gas–pressure distributions for concrete with 0 and 1.5 kg/m^3 PP-fibers (results for t=0, 2, 10, 30, 90, 180 min).

the evaporable water to occur only at the location of a chosen T-isotherm. Accordingly, the amount of moles vaporizing per unit time, $\mathrm{d}n_{\mathrm{Vap}}/\mathrm{d}t$ [mol/s], can be determined from the velocity of this T-isotherm (see Appendix B), with

$$\frac{\mathrm{d}n_{\mathrm{Vap}}}{\mathrm{d}t} = \frac{Am_{\mathrm{w0}}}{M_{\mathrm{w}}} v_T, \tag{8}$$

where A=1 m^2 is the surface area, m_{w0} [(kg water)/(m^3 concrete)] is the amount of evaporable water, and M_{w}=0.018 kg/mol represents the molar mass of liquid water (see, e.g., Ref. [36]).

The pressure build-up caused by the vaporization of evaporable water is reduced by advection of water vapor towards the heated surface.[6] The respective molar flux $\mathrm{d}n_{\mathrm{Adv}}/\mathrm{d}t$ [mol/s] is given by (see Appendix C)

$$\frac{\mathrm{d}n_{\mathrm{Adv}}}{\mathrm{d}t} = \frac{p^{\mathrm{gws}}}{RT}\frac{Ak}{\eta^{\mathrm{gw}}}\frac{(p^{\mathrm{gws}}-p_0)}{x_T}, \tag{9}$$

with p^{gws} [Pa] as the saturation-vapor pressure corresponding to the temperature T [K] of the chosen T-isotherm (see, e.g., Ref. [36]), R=8.31 J/(mol K) as the gas constant, and η^{gw} [Pa s] as the dynamic viscosity of water vapor. In accordance to Refs. [25,27],[7] the permeability k [m^2] appearing in Eq. (9) is set equal to the intrinsic permeability k_{int} [m^2].

For the analysis of the location of the T-isotherm and the production and advection, respectively, of water vapor, the concrete properties given in Tables 2 and 4 are employed. As reported in Ref. [7], the maximum values for the vapor pressure are found within 170 ≤ T ≤ 210 °C for normal-strength concrete. Hence, in the following, the propagation of three T-isotherms, with T=160, 190, and 220 °C, into the concrete block is investigated. Following the Clausius–Clapeyron equation, the saturation-vapor pressure p^{gws} [Pa] (see Eq. (9)) corresponding to T=160, 190, and 220 °C is $p^{\mathrm{gws}}=0.62\cdot10^6$, $1.25\cdot10^6$, and $2.32\cdot10^6$ Pa, respectively (see Table 4 and, e.g., Ref. [36]). The dynamic viscosity of water vapor is chosen to be constant, with $\eta^{\mathrm{gw}}=15.78\cdot10^{-6}$ Pa s, which corresponds to T=200 °C.

Table 4
Input parameters for investigation of governing mass fluxes to assess the risk of spalling

Input parameter	Value	Source
Boundary-temperature increase c for t<600; 900 s [°C/s]	0.80; 0.25	Fig. 15
Initial amount of evaporable water (determined at 105 °C) m_{w0} [(kg water)/(m^3 concrete)]	56.7	[10]
Atmospheric pressure p_0 [Pa]	101,325	–
Saturation-vapor pressure p^{gws} for T=160; 190; 220 °C [10^6 Pa]	0.62; 1.25; 2.32	[36]
Dynamic viscosity of water vapor η^{gw} [Pa s]	$15.78\cdot10^{-6}$	[36]
Intrinsic permeability k_{int} of concrete with 0 kg/m^3 PP-fibers for T=160; 190; 220 °C [10^{-16} m^2]	4.80; 6.44; 8.64	Fig. 6
Intrinsic permeability k_{int} of concrete with 1.5 kg/m^3 PP-fibers for T=160; 190; 220 °C [10^{-16} m^2]	14.7; 25.1; 34.3	Fig. 7

Fig. 20 shows the location of the considered T-isotherms, x_T [m], as a function of time. Since the thermal properties are assumed to be independent of the fiber content, x_T is the same for concrete with and without PP-fibers. Based on the location of the T-isotherm, the respective values for $\mathrm{d}n_{\mathrm{Vap}}/\mathrm{d}t$ and $\mathrm{d}n_{\mathrm{Adv}}/\mathrm{d}t$ [mol/s] are evaluated according to Eqs. (8) and (9) for concrete with and without fibers.

The influence of the fiber content, i.e., of the permeability k_{int} [m^2], on the spalling behavior is illustrated in Figs. 21 and 22. Whereas the plots of the amount of vaporized moles, $\mathrm{d}n_{\mathrm{Vap}}/\mathrm{d}t$ [mol/s], are the same for concrete with and without PP-fibers (x_T [m] and, hence, v_T [m/s] are independent of the fiber content, see Fig. 20), $\mathrm{d}n_{\mathrm{Adv}}/\mathrm{d}t$ depends on the permeability, which is the only material parameter affected by the PP-fibers within the chosen mode of estimating the vapor transport.

For the analysis of concrete without PP-fibers, the amount of moles that can be advected towards the heated surface becomes smaller than the amount of vaporized moles for T=160 °C (see Fig. 21). This results in a pressure build-up at the actual location of the T-isotherm (x_T=2.03 cm). When the pressure exceeds the material strength, which itself decreases with increasing

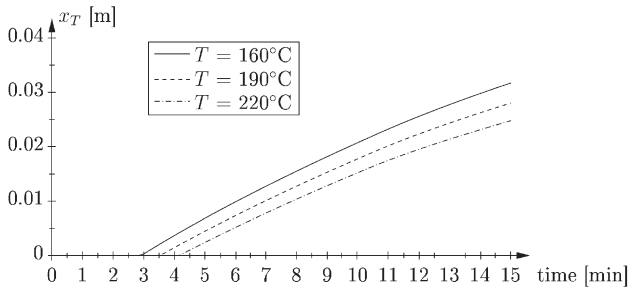

Fig. 20. History of location of T-isotherm (input parameters: see Tables 2 and 4).

[6] Hereby, the "moisture clog" shown in Fig. 2(c) is assumed to be present at the location of the chosen T-isotherm and, therefore, hinders vapor advection further into the concrete. Hence, the whole amount of water vapor must be transported towards the heated surface.

[7] Since instantaneous vaporization is assumed in this study and, hence, no liquid water is present in the region between the vaporization front and the heated surface, the relative permeability used in Refs. [25,27] is set equal to one.

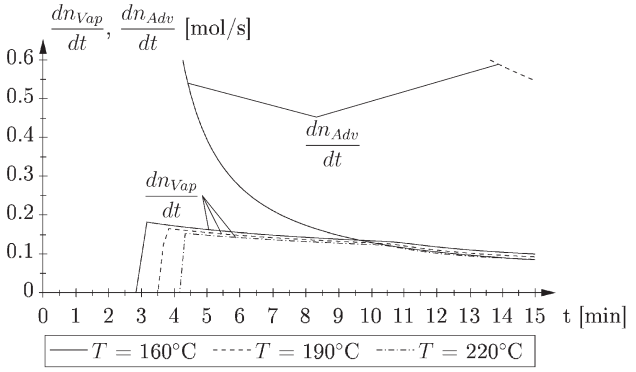

Fig. 21. History of dn_{Vap}/dt and dn_{Adv}/dt for concrete with 0 kg/m^3 PP-fibers (input parameters: see Tables 2 and 4).

temperature, spalling occurs. For $T=190$ and 220 °C, the higher values of the permeability k_{int} and the saturation-vapor pressure p^{gws} (the latter results in a larger pressure gradient) yield values for dn_{Adv}/dt larger than dn_{Vap}/dt for the whole duration of the analysis. In case of $T=220$ °C, the amount of advected moles is at least 32 times larger than the amount of vaporized moles. According to Fig. 21, the history of dn_{Vap}/dt exhibits a sharp increase when the chosen temperature isotherm enters the concrete structure. On the other hand, the evolution of dn_{Adv}/dt decreases fast when the chosen T-isotherm progresses further into the concrete, which results in an intersection with the corresponding dn_{Vap}/dt curve most likely shortly after 3–4 min of fire loading, see Fig. 21. This time span agrees well with the start of spalling within the fire experiments reported in Ref. [10].

The plot for concrete with 1.5 kg/m^3 PP-fibers (Fig. 22), on the other hand, shows a different performance. For all chosen temperatures, the amount of advected moles is larger than the amount of vaporized moles. For $T=160$ °C, dn_{Adv}/dt is more than twice as large as dn_{Vap}/dt. For $T=190$ and 220 °C, the ratio is even larger (at least factor 23 and 128, respectively). Hence, no pressure build-up will occur and, therefore, the risk of spalling is considerably reduced. This conclusion agrees with the outcome of the experimental program outlined in Ref. [10].

5. Conclusions

Motivated by recent results from large-scale fire experiments showing a great influence of the amount of polypropylene (PP) fibers on the spalling behavior of concrete, permeability and mercury-intrusion-porosimetry (MIP) experiments were conducted on in-situ concrete. Based on the obtained results, the following conclusions can be drawn:

- For pre-heating temperatures lower than 140 °C, the permeability of concrete with 1.5 kg/m^3 PP-fibers was three to four times larger than the permeability of concrete without fibers with decreasing difference for increasing temperature. This is contrary to results obtained from laboratory-cast specimens reported in the open literature, where this difference is considerably smaller. While the values for the total pore volume, which showed no distinct difference between concrete with and without PP-fibers, could not explain the observed difference, the pore volume within pore radii of $10^3 \le r \le 10^5$ nm was considerably larger (twice as large) for concrete with PP-fibers compared to concrete without fibers. Since this pore-size range corresponds to the thickness of interfacial transition zones (ITZ), the PP-fibers apparently introduce additional ITZ, resulting in a higher permeability for fiber-reinforced concrete. This effect is amplified for the considered in-situ concrete. On-site conditions, characterized by the reduced workability and the lower effect of densification in case of PP-fiber reinforced concrete, seem to influence the pore structure and/or the characteristics of the ITZ.
- For temperatures between 140 and 200 °C, the difference between the permeability of concrete with and without PP-fibers increased, reaching again a factor of four. Hence, in case of the tested in-situ concrete, the effect of melting of PP-fibers had equal impact as the difference in the low-temperature permeability. Nevertheless, the investigation of the pore-size distributions of concrete with and without fibers revealed the development of pores with radii within $6 \le r \le 10$ μm, which supported the theory of increased permeability in consequence of melting of the PP-fibers ($\phi \approx 18$ μm) at $T \approx 170$ °C.

Temperature measurements from the mentioned large-scale fire experiments were compared to numerical results from different FE analyses. In general, the agreement between numerical and experimental results improved with increasing grade of complexity of the simulation. Disregard of mass transport in the analysis resulted in an overestimation of the experimentally obtained temperatures in regions close to the heated surface. The numerical analyses considering mass transport showed gas pressures almost twice as large in case of concrete with 0 kg/m^3 PP-fibers and an increase of the saturation (exceeding the initial value), indicating the formation of a moisture clog.

Taking into account that the mode of prescribing the temperature at the heated surface had the largest impact on the numerically obtained temperature distribution, the risk of spalling was investigated by a two-step analysis, considering (i) the experimentally obtained values for the permeability and (ii)

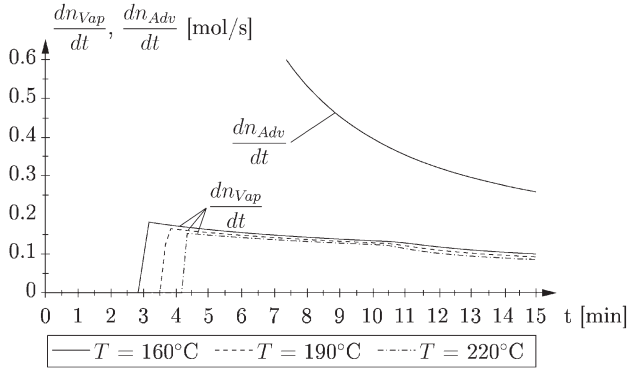

Fig. 22. History of dn_{Vap}/dt and dn_{Adv}/dt for concrete with 1.5 kg/m^3 PP-fibers (input parameters: see Tables 2 and 4).

the shape of the gas–pressure distribution within the heated concrete obtained from the coupled numerical simulation. In the first step, the progress of a chosen temperature isotherm into the concrete member was determined from the thermal analysis. In the second step, the water vapor production as a function of time (which was calculated from the velocity of a chosen temperature isotherm) was compared to the water vapor advection towards the heated surface. In case of concrete with 0 kg/m^3 PP-fibers, the amount of vaporized water became larger than the respective amount of vapor that can be transported towards the heated surface, indicating a pressure build-up and, hence, an increased risk of spalling. For concrete with 1.5 kg/m^3 PP-fibers, this phenomenon was not observed. Moreover, indications concerning the start of spalling could be extracted from the presented analysis scheme. The sharp increase of the amount of vaporized water $\mathrm{d}n_{\mathrm{Vap}}/\mathrm{d}t$ at the time instant the chosen temperature isotherm enters the concrete, on the one hand, and the fast decrease of the amount of advected vapor $\mathrm{d}n_{\mathrm{Adv}}/\mathrm{d}t$ when this isotherm progresses further into the concrete, on the other hand, led to the conclusion that the intersection of the histories of $\mathrm{d}n_{\mathrm{Vap}}/\mathrm{d}t$ and $\mathrm{d}n_{\mathrm{Adv}}/\mathrm{d}t$ most likely occurs shortly after the chosen temperature isotherm has entered the concrete structure. The described sharp increase of $\mathrm{d}n_{\mathrm{Vap}}/\mathrm{d}t$ took place after 3–4 min of fire loading, which agrees well with the start of spalling in case of concrete with 0 kg/m^3 PP-fibers observed within large-scale fire experiments [10]. In case of concrete reinforced with PP-fibers, on the other hand, the higher permeability resulted in a reduced spalling risk, which is in agreement with results from large-scale fire experiments reported in Refs. [10,31].

Acknowledgments

The authors are grateful to Wolfgang Kusterle (University of Applied Sciences, Regensburg, Germany) and Wolfgang Lindlbauer (Vienna, Austria) for helpful support in the research project “Fire Resistance of Fiber-reinforced, Reinforced, and Prestressed Concrete” (“Brandbeständigkeit von Faser-, Stahl- und Spannbeton”), sponsored by the Austrian Ministry for Transportation and the OEBB-Infrastruktur Bau AG (Vienna, Austria). They also wish to thank Ulrich Schneider and Johannes Horvath (both from Vienna University of Technology, Austria) for assistance during the MIP experiments. Furthermore, the authors thank Bernhard A. Schrefler and Francesco Pesavento (University of Padova, Italy) and Dariusz Gawin (Technical University of Łódz, Poland) for providing access to the finite element tool “HITECOSP” and for helpful support during computational work. Financial support by the Austrian Science Fund (FWF) via project P16517-N07 “Transport processes in concrete at high temperatures” is gratefully acknowledged.

Appendix A. Governing equations for the simulation of heat and mass transport in heated concrete

In the coupled analyses presented in Section 3, the following governing equations are solved in a fully coupled manner with respect to the three main state variables, i.e., capillary pressure p^{c}, gas pressure p^{g}, and temperature T:

(1) Mass balance equation for the water phase (water vapor and liquid water, involving the solid mass balance equation):

$$\begin{aligned} &n(\rho^{\mathrm{w}}-\rho^{\mathrm{gw}})\frac{\partial S_{\mathrm{w}}}{\partial t}+n(1-S_{\mathrm{w}})\frac{\partial \rho^{\mathrm{gw}}}{\partial t}+nS_{\mathrm{w}}\frac{\partial \rho^{\mathrm{w}}}{\partial t}-\beta_{\mathrm{swg}}\frac{\partial T}{\partial t}\\ &\quad+\mathrm{div}[n(1-S_{\mathrm{w}})\rho^{\mathrm{gw}}\mathrm{v}^{\mathrm{gs}}]+\mathrm{div}[nS_{\mathrm{w}}\rho^{\mathrm{w}}\mathrm{v}^{\mathrm{ws}}]+\mathrm{div}\mathrm{J}_{\mathrm{g}}^{\mathrm{gw}}\\ &\quad=-\frac{(1-n)[\rho^{\mathrm{gw}}(1-S_{\mathrm{w}})+\rho^{\mathrm{w}}S_{\mathrm{w}}]}{\rho^{\mathrm{s}}}\frac{\partial \rho^{\mathrm{s}}}{\partial \xi}\frac{\partial \xi}{\partial t}\\ &\qquad+[\rho^{\mathrm{gw}}(1-S_{\mathrm{w}})+\rho^{\mathrm{w}}S_{\mathrm{w}}]\frac{\dot{m}_{\mathrm{dehydr}}}{\rho^{\mathrm{s}}}-\dot{m}_{\mathrm{dehydr}}; \end{aligned} \tag{A.1}$$

(2) Mass balance equation for the dry air phase (involving the solid mass balance equation):

$$\begin{aligned} &-n\rho^{\mathrm{ga}}\frac{\partial S_{\mathrm{w}}}{\partial t}+n(1-S_{\mathrm{w}})\frac{\partial \rho^{\mathrm{ga}}}{\partial t}-\rho^{\mathrm{ga}}(1-n)(1-S_{\mathrm{w}})\beta_{\mathrm{s}}\frac{\partial T}{\partial t}\\ &\quad+\mathrm{div}[n(1-S_{\mathrm{w}})\rho^{\mathrm{ga}}\mathrm{v}^{\mathrm{gs}}]+\mathrm{div}\mathrm{J}_{\mathrm{g}}^{\mathrm{ga}}\\ &\quad=-\frac{(1-n)\rho^{\mathrm{ga}}(1-S_{\mathrm{w}})}{\rho^{\mathrm{s}}}\frac{\partial \rho^{\mathrm{s}}}{\partial \xi}\frac{\partial \xi}{\partial t}+\rho^{\mathrm{ga}}(1-S_{\mathrm{w}})\frac{\dot{m}_{\mathrm{dehydr}}}{\rho^{\mathrm{s}}}; \end{aligned} \tag{A.2}$$

(3) Enthalpy balance equation:

$$\begin{aligned} &(\rho c_{\mathrm{p}})_{\mathrm{eff}}\frac{\partial T}{\partial t}+[n(1-S_{\mathrm{w}})\rho^{\mathrm{g}}c_{\mathrm{p}}^{\mathrm{g}}\mathrm{v}^{\mathrm{gs}}\\ &\quad+nS_{\mathrm{w}}\rho^{\mathrm{w}}c_{\mathrm{p}}^{\mathrm{w}}\mathrm{v}^{\mathrm{ws}}]\mathrm{grad}T-\mathrm{div}(\lambda_{\mathrm{eff}}\mathrm{grad}T)\\ &\quad=-\dot{m}_{\mathrm{vap}}h+\dot{m}_{\mathrm{dehydr}}l_{\xi}^{\mathrm{w}}. \end{aligned} \tag{A.3}$$

For details, the reader is referred to, e.g., Refs. [25–28]. The boundary conditions are defined by (i) prescribed values for the capillary and gas pressure ($\overline{p}^{\mathrm{c}}$ and $\overline{p}^{\mathrm{g}}$), and for the temperature ($\overline{T}$) (Dirichlet’s BC), (ii) prescribed mass fluxes (q^{w}, q^{gw}, and q^{ga}) and heat fluxes (q^{T}) (Neumann’s BC), or (iii) mass and heat transfer fluxes (Cauchy’s BC) introducing mass and heat-transfer parameters (convective water vapor flux $q_{\mathrm{c}}^{\mathrm{gw}}$ and convective and radiative heat fluxes, $q_{\mathrm{c}}^{\mathrm{T}}$ and $q_{\mathrm{r}}^{\mathrm{T}}$, respectively). To complete the model in order to solve the governing equations (Eqs. (A.1)–(A.3)), the following constitutive relationships are introduced [26]:

- Kelvin equation (defining the relative humidity RH),
- Clausius–Clapeyron equation (relationship between saturation-vapor pressure p^{gws} and temperature T),
- Young–Laplace equation (relation between capillary pressure p^{c} and pore radius r),
- Clapeyron equation (ideal gas law),
- Dalton’s law (definition of partial pressures of water vapor, p^{gw} and of dry air, p^{ga}),
- Darcy’s law (pressure-driven flux of water and vapor),
- Fick’s law (diffusional flux of water vapor in dry air).

The resulting set of governing equations is discretized in space. The so-obtained (non-linear) finite element formulation is solved by means of a Newton–Raphson iteration scheme [26,27].

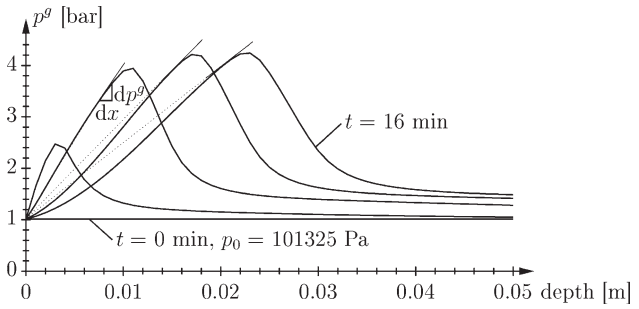

Fig. C.1. Gas–pressure distribution at various time instants (t=0, 4, 8, 12, 16 min) obtained from numerical analysis presented in Section 3 (in the region of the maximum gas pressure p^g, the partial pressure of dry air is almost zero and, hence, $\mathrm{d}p^g/\mathrm{d}x = \mathrm{d}p^{gw}/\mathrm{d}x$ is valid).

For the solution of the thermal problem only, Eq. (A.3) is reduced to

$$\rho_c c_p \frac{\partial T}{\partial t} - \mathrm{div}(\lambda \mathrm{grad} T) = 0. \tag{A.4}$$

In this case, Eqs. (A.1) and (A.2) are disregarded.

Appendix B. Determination of vaporizing water

Assuming instantaneous vaporization at the location of a chosen T-isotherm (see Section 4), with $T \geq 100$ °C, an infinitesimal progress of this isotherm by $\mathrm{d}x_T$ [m] is associated with the vaporization of evaporable water, given by

$$\mathrm{d}m_{\mathrm{Vap}}\ [\mathrm{kg}] \propto \mathrm{d}x_T = \frac{\partial x_T}{\partial t}\mathrm{d}t = v_T \mathrm{d}t\ [\mathrm{m}], \tag{B.1}$$

where v_T [m/s] represents the velocity of the T-isotherm, as defined in Section 4. Rewriting Eq. (B.1) for a surface area A=1 m^2 and introducing the water content w [(kg water)/(kg concrete)] and the concrete density ρ_c [(kg concrete)/(m^3 concrete)], one gets

$$\mathrm{d}m_{\mathrm{Vap}} = A w \rho_c v_T \mathrm{d}t. \tag{B.2}$$

The number of moles $\mathrm{d}n_{\mathrm{Vap}}(l)$ [mol] corresponding to $\mathrm{d}m_{\mathrm{Vap}}$ [kg] is obtained from the molar mass of liquid water M_w [kg/mol], with M_w=0.018 kg/mol (see, e.g., Ref. [36]), giving

$$\mathrm{d}n_{\mathrm{Vap}}(l) = \frac{\mathrm{d}m_{\mathrm{Vap}}}{M_w} = \frac{A m_{w0}}{M_w} v_T \mathrm{d}t, \tag{B.3}$$

where $m_{w0} = w\rho_c$ [(kg water)/(m^3 concrete)] is the amount of liquid (evaporable) water present within the concrete. Since the vaporization is assumed to occur instantaneously at the location of the T-isotherm, the number of moles of water is the same before and after vaporization.[8] Considering $\mathrm{d}n_{\mathrm{Vap}}(l) = \mathrm{d}n_{\mathrm{Vap}}(v) = \mathrm{d}n_{\mathrm{Vap}}$ yields the amount of moles vaporizing per unit time, $\mathrm{d}n_{\mathrm{Vap}}/\mathrm{d}t$ [mol/s], as (see also Eq. (8))

$$\frac{\mathrm{d}n_{\mathrm{Vap}}}{\mathrm{d}t} = \frac{A m_{w0}}{M_w} v_T. \tag{B.4}$$

Appendix C. Determination of the water vapor that can be advected towards the heated surface

As mentioned in Section 4, the whole amount of water that vaporizes at a chosen T-isotherm is transported towards the heated surface by advection. The respective water vapor flux Q_{Adv} [m^3/s] is given by Darcy's law as

$$Q_{\mathrm{Adv}} = \frac{Ak}{\eta^{gw}}\left(-\frac{\partial p^{gw}}{\partial x}\right), \tag{C.1}$$

with A=1 m^2 as the surface area, k [m^2] as the permeability, η^{gw} [Pa s] as the dynamic viscosity of water vapor (which is temperature-dependent, ranging from 12.28×10^{-6} Pa s at 100 °C to 17.59×10^{-6} Pa s at 250 °C; see, e.g., Ref. [36]), and $\partial p^{gw}/\partial x$ [Pa/m] as the pressure gradient. Clapeyron's law for ideal gases is used to relate the volumetric flux $Q_{\mathrm{Adv}} = \mathrm{d}V_{\mathrm{Adv}}/\mathrm{d}t$ [m^3/s] to the molar flux $\mathrm{d}n_{\mathrm{Adv}}/\mathrm{d}t$ [mol/s], reading

$$n_{\mathrm{Adv}} = \frac{p^{gws}}{RT}V_{\mathrm{Adv}} \rightarrow \frac{\mathrm{d}n_{\mathrm{Adv}}}{\mathrm{d}t} = \frac{p^{gws}}{RT}\frac{\mathrm{d}V_{\mathrm{Adv}}}{\mathrm{d}t} = \frac{p^{gws}}{RT}Q_{\mathrm{Adv}}, \tag{C.2}$$

where p^{gws} [Pa] is the saturation-vapor pressure related to the temperature T [K] of the chosen T-isotherm[9] and R=8.31 J/(mol K) is the gas constant. Inserting Eq. (C.1) into Eq. (C.2) gives the molar flux for the considered T-isotherm as

$$\frac{\mathrm{d}n_{\mathrm{Adv}}}{\mathrm{d}t} = \frac{p^{gws}}{RT}\frac{Ak}{\eta^{gw}}\left(-\frac{\partial p^{gw}}{\partial x}\right). \tag{C.3}$$

Based on the numerical results presented in this work (see Fig. C.1) as well as experimental results reported in the open literature (see, e.g., Ref. [7]), the pressure distribution at the location of the maximum pressure[10] may be estimated by a linear function, yielding the pressure gradient as a function of the actual location of a chosen T-isotherm, x_T [m], as $-(\partial p^{gw}/\partial x) \approx (p^{gws} - p_0)/x_T$. Finally, Eq. (C.3) becomes (see also Eq. (9))

$$\frac{\mathrm{d}n_{\mathrm{Adv}}}{\mathrm{d}t} = \frac{p^{gws}}{RT}\frac{Ak}{\eta^{gw}}\frac{(p^{gws} - p_0)}{x_T}, \tag{C.4}$$

where p_0 [Pa] is the pressure at the heated surface.

References

[1] Z.P. Bažant, Analysis of pore pressure, thermal stress and fracture in rapidly heated concrete, in: L.T. Phan, N.J. Carino, D. Duthinh,

[8] Hereby, the amount of moles of moist air (mixture of dry air and water vapor) present prior to vaporization of evaporable water is neglected [33].

[9] The correspondence between the vapor pressure and the temperature according to the Clausius–Clapeyron equation (see, e.g., Ref. [36]) was also observed in fire experiments on normal-strength concrete presented in Ref. [7].

[10] The numerical results show that in the region of the maximum gas pressure p^g, the partial pressure of dry air is almost zero and, hence, $p^g = p^{gw}$ is valid.

E. Garboczi (Eds.), Proceedings of the International Workshop on Fire Performance of High-Strength Concrete, NIST, Gaithersburg, Maryland, 1997, pp. 155–164.
[2] F.-J. Ulm, O. Coussy, Z. Bažant, The "Chunnel" fire I: chemoplastic softening in rapidly heated concrete, Journal of Engineering Mechanics (ASCE) 125 (3) (1999) 272–282.
[3] G. Khoury, C.E. Majorana, Thermo-hydral behaviour, in: G. Khoury, C.E. Majorana (Eds.), Effect of Heat on Concrete, International Centre for Mechanical Science, Udine, 2003, pp. 1–18.
[4] C. Meyer-Ottens, Zur Frage der Abplatzungen an Betonbauteilen aus Normalbeton bei Brandbeanspruchung [Spalling of normal-strength concrete structures under fire loading], Ph.D. thesis, Braunschweig University of Technology, Braunschweig, Germany, in German (1972).
[5] Y. Anderberg, Spalling phenomena in HPC and OC, in: L.T. Phan, N.J. Carino, D. Duthinh, E. Garboczi (Eds.), Proceedings of the International Workshop on Fire Performance of High-Strength Concrete, NIST, Gaithersburg, Maryland, 1997, pp. 69–73.
[6] G.R. Consolazio, M.C. McVay, J.W. Rish III, Measurement and prediction of pore pressure in cement mortar subjected to elevated temperature, in: L. T. Phan, N.J. Carino, D. Duthinh, E. Garboczi (Eds.), Proceedings of the International Workshop on Fire Performance of High-Strength Concrete, NIST, Gaithersburg, Maryland, 1997, pp. 125–148.
[7] P. Kalifa, F.-D. Menneteau, D. Quenard, Spalling and pore pressure in HPC at high temperatures, Cement and Concrete Research 30 (2000) 1915–1927.
[8] U. Schneider, J. Horvath, Abplatzverhalten an Tunnelinnenschalenbeton [Spalling of concrete for tunnel linings], Beton- und Stahlbetonbau 97 (4) (2002) 185–190 (in German).
[9] K.D. Hertz, Limits of spalling of fire-exposed concrete, Fire Safety Journal 38 (2003) 103–116.
[10] W. Kusterle, W. Lindlbauer, G. Hampejs, A. Heel, P.-F. Donauer, M. Zeiml, W. Brunnsteiner, R. Dietze, W. Hermann, H. Viechtbauer, M. Schreiner, R. Vierthaler, H. Stadlober, H. Winter, J. Lemmerer, E. Kammeringer, Brandbeständigkeit von Faser-, Stahl- und Spannbeton [Fire resistance of fiber-reinforced, reinforced, and prestressed concrete], Tech. Rep. 544, Bundesministerium für Verkehr, Innovation und Technologie, Vienna, 2004 (in German).
[11] W. Lindlbauer, M. Zeiml, Forschungsvorhaben Brandbeständigkeit von Faser-, Stahl- und Spannbeton — Aufgabenstellung und Versuchsdurchführung [Research project on fire resistance of fiber-reinforced, reinforced, and prestressed concrete — concept, formulation, and implementation of experiments], Schriftenreihe der Österreichischen Vereinigung für Beton- und Bautechnik 50 (2002) 67–74 (in German).
[12] P. Kalifa, G. Chéné, C. Gallé, High temperature behaviour of HPC with polypropylene fibres: from spalling to microstructure, Cement and Concrete Research 31 (2001) 1487–1499.
[13] W. Kusterle, N.-V. Waubke, Die Brandbeständigkeit von Faser-, Stahl- und Spannbeton [Fire resistance of fiber-reinforced, reinforced, and prestressed concrete], Schriftenreihe der Österreichischen Vereinigung für Beton-und Bautechnik 47 (2001) 89–96 (in German).
[14] G.R. Consolazio, M.C. McVay, J.W. Rish III, Measurement and prediction of pore pressure in saturated cement mortar subjected to radiant heating, ACI Materials Journal 95 (5) (1998) 525–536.
[15] Österreichisches Normungsinstitut, ÖNORM B4200-10, Beton — Herstellung, Verwendung und Gütenachweis [Concrete — Production, Use and Verification of Quality], 1996 (in German).
[16] M. Zeiml, R. Lackner, D. Leithner, J. Eberhardsteiner, A novel experimental technique for determination of the permeability of concrete subjected to high temperature, Cement and Concrete Research, submitted for publication.
[17] L.J. Klinkenberg, The permeability of porous media to liquids and gases, American Petroleum Institute, Drilling Production Practice (1941) 200–213.
[18] Y. Wang, V.C. Li, S. Backer, Tensile properties of synthetic fiber reinforced mortar, Cement and Concrete Composites 12 (1990) 29–40.
[19] M.A. Sanjuán, A. Moragues, A testing method for measuring plastic shrinkage in polypropylene fibre reinforced mortars, Materials Letters 21 (1994) 239–246.
[20] H.A. Mesbah, F. Buyle-Bodin, Efficiency of polypropylene and metallic fibres on control of shrinkage and cracking of recycled aggregate mortars, Construction and Building Materials 13 (1999) 439–447.
[21] K. Wille, H. Schneider, Investigation of fibre reinforced high strength concrete (HSC) under fire, particularly with regard to the real behavior of polypropylene fibres, Leipzig Annual Civil Engineering Report, vol. 7, Institut für Massivbau und Baustofftechnologie, Leipzig, Germany, 2002, pp. 61–70 (in German).
[22] D. Leithner, Experimental investigation of concrete subjected to fire loading: micromechanical approach for determination of the permeability, Master's thesis, Vienna University of Technology, Vienna, Austria (2004).
[23] E.J. Garboczi, D.P. Bentz, Multiscale analytical/numerical theory of the diffusivity of concrete, Advanced Cement Based Materials 8 (1998) 77–88.
[24] G. Bye, Portland Cement, 2nd Edition, Thomas Telford Publishing, London, 1999.
[25] R. Lewis, B. Schrefler, The Finite Element Method in the Static and Dynamic Deformation and Consolidation of Porous Media, 2nd Edition, John Wiley & Sons, Chichester, 1998.
[26] D. Gawin, C.E. Majorana, B.A. Schrefler, Numerical analysis of hygro-thermal behaviour and damage of concrete at high temperature, Mechanics of Cohesive–Frictional Materials 4 (1999) 37–74.
[27] D. Gawin, F. Pesavento, B.A. Schrefler, Modelling of hygro-thermal behaviour of concrete at high temperature with thermo-chemical and mechanical material degradation, Computer Methods in Applied Mechanics and Engineering 192 (2003) 1731–1771.
[28] B.A. Schrefler, Multiphase flow in deforming porous material, International Journal for Numerical Methods in Engineering 60 (2004) 27–50.
[29] J. Horvath, Beiträge zum Brandverhalten von Hochleistungsbeton [Contributions to the behavior of high-performance concrete under fire], Ph.D. thesis, Vienna University of Technology, Vienna, Austria, in German (2003).
[30] P. Nischer, J. Steigenberger, H. Wiklicky, Praxisverhalten von erhöht brandbeständigem (Innenschalen-) Beton (EBB) [Practical use of fire resistant concrete for tunnel linings], Tech. Rep., FFF-project no. 806201, Forschungsinstitut der Vereinigung der österreichischen Zementindustrie (VÖZ), Vienna, 2004 (in German).
[31] J. Horvath, U. Schneider, U. Diederichs, Brandverhalten von Hochleistungsbetonen [Fire resistance of high performance concrete], Tech. Rep. 11, Vienna University of Technology, Vienna, Austria, 2004 (in German).
[32] Österreichisches Normungsinstitut, Vienna, ENV1992-1-2, Eurocode 2 — Planung von Stahlbeton- und Spannbetontragwerken — Teil 1–2: Allgemeine Regeln — Tragwerksbemessung für den Brandfall [Eurocode 2 — Design of Concrete Structures — Part 1–2: General Rules — Structural Fire Design], 1997 (in German).
[33] M. Zeiml, Analytical and numerical modeling of heat and water-vapor transport in concrete subjected to fire loading, Master's thesis, Vienna University of Technology, Vienna, Austria (2004).
[34] U. Grigull, H. Sandner, Wärmeleitung [Heat Conduction], 2nd Edition, Springer, Berlin, 1990 (in German).
[35] C.-E. Hagentoft, Elementary building physics, Tech. Rep., 4, Chalmers University of Technology, Göteborg, Sweden, 2000.
[36] W. Blanke, M. Biermann, Thermophysikalische Stoffgrößen [Thermophysical material parameters], vol. 1, Springer, Berlin, 1989 (in German).